Influence of water table fluctuations and temperature on LNAPL distribution in heterogeneous porous media

Lazzat Amangaliyeva, Maxime Cochennec, Sagyn Omirbekov, E.D. van Hullebusch, Stéfan Colombano, Aizhan Ibrayeva, Dorian Davarzani

To cite this version:

Lazzat Amangaliyeva, Maxime Cochennec, Sagyn Omirbekov, E.D. van Hullebusch, Stéfan Colombano, et al.. Influence of water table fluctuations and temperature on LNAPL distribution in heterogeneous porous media. Integrated Environmental Assessment and Management, 2025, ⟨10.1093/inteam/vjaf172⟩. ⟨hal-05396191⟩

HAL Id: hal-05396191
https://brgm.hal.science/hal-05396191v1

Submitted on 13 Jan 2026

ABSTRACT

The remediation of soils and aquifers contaminated by Light Non-Aqueous Phase Liquid (LNAPL) relies on a precise understanding of the LNAPL distribution above the water table. This study investigates the impact of groundwater table fluctuations and temperature change on LNAPL redistribution in a heterogeneous porous medium through laboratory-scale experiments. Experiments were conducted in a two-dimensional tank simulating aquifer condition, using diesel fuel as the LNAPL. The reservoir filled with coarse sand and fine sand low-permeability lenses, reproduced the subsurface heterogeneity. Following LNAPL infiltration from the top, controlled drainage and imbibition cycles simulated water table fluctuations. Experiments were conducted at 10°C and 20°C to characterize temperature effects. Fluid behavior was monitored using Time Domain Reflectometry (TDR) probes and high-resolution image analysis. TDR measurements provided quantitative dielectric permittivity data, which were converted to saturation profiles. Simultaneously, an image processing approach using the Biodock platform based on artificial intelligence and OpenCV was used to visualize the spatial distribution of LNAPL, water, and air. Applying the two methods allowed integrated methodology and a detailed understanding of the dynamics driving LNAPL migration. Results show that water table fluctuations significantly affect LNAPL redistribution, with each imbibition cycle leading to LNAPL entrapment in the capillary fringe due to wettability changes and capillary barriers. Higher temperature increased the mobility of LNAPL by reducing its viscosity, resulting in more efficient fluid displacement during drainage. This highlights the importance of studying the fate and transport of pollutants in the laboratory under temperature conditions relevant to the aquifers. Low-permeability lenses further modulated LNAPL migration, emphasizing subsurface heterogeneity critical role. Overall, the comprehensive experimental design combining TDR and advanced image analysis provides insight into the mechanisms of LNAPL behavior under dynamic environmental conditions and hints at further improvements for predictive models and remediation strategies in contaminated subsurface environments.

Keywords: Light non-aqueous phase liquid (LNAPL), water table fluctuation, temperature influence, AI-based image analysis, time domain reflectometry

INTRODUCTION

Light Non-Aqueous Phase Liquids (LNAPLs), such as refined petroleum, pose a significant environmental and human health risk when they contaminate soil and groundwater (Newell, 1995). These pollutants are often generated from industrial spills, storage leaks, and gas station accidents. Once in the subsurface, LNAPL interacts with the soil matrix and groundwater, undergoing processes such as trapping, sorption, volatilization, dissolution, and biodegradation. Due to their lower density than water and limited solubility, LNAPLs tend to accumulate at the water table, creating long-term contamination sources (Atteia et al., 2017; Cavelan et al., 2022; Rivett et al., 2014). This persistent pollution threatens groundwater quality-a critical resource for drinking water supply, agriculture, and industrial processes such as cooling and heating-that is vital to the surrounding ecosystem. Additionally, some hydrocarbon compounds have toxic or carcinogenic properties, posing direct risks to human health. Managing LNAPLs contamination requires a comprehensive understanding of the factors influencing their behavior in subsurface environments. Water table fluctuations, soil heterogeneities, and temperature variations are three key factors influencing the fate and transport of LNAPLs in the critical zone (i.e., the zone of water table fluctuation and the capillary fringe). Their individual and combined effects require further characterization. While several studies have explored each mechanism separately (Alazaiza et al., 2020; Cavelan et al., 2024; Koohbor et al., 2023; Zuo et al., 2021), no study—to the best of the authors' knowledge—has investigated all three factors simultaneously using a unified experimental setup integrating instrumentation and imaging.

Fluctuations in the water table—driven by seasonal precipitation, recharge, flooding, pumping, or long-term climatic shifts—significantly impact fluid distribution and interactions in porous media. When the water table rises, previously unsaturated zones become saturated, potentially mobilizing trapped LNAPL into the free or the dissolved phase, increasing the risk of contamination spreading. Conversely, when the water table drops, formerly saturated zones transition into the vadose zone, trapping LNAPL as residual saturation in the pore spaces. This process forms a ‘smear zone’, which acts as a long-term contamination source. These fluctuations create complex three-phase flow dynamics in the capillary fringe, further complicated by hysteresis effects—meaning the system’s state (e.g., saturation) at a given time depends on whether the process involves drainage or imbibition. Along with saturation, key LNAPL transport properties—such as relative permeability and capillary pressure—also vary depending on the flow direction (Blunt, 2016; Whitaker, 1986).

Among the studies examining the effect of water table fluctuations, Oostrom et al., (2006) analyzed the impact of a 50.0 cm rise in water table level over 50 min on residual LNAPL. Using dual-energy gamma radiation to monitor LNAPL saturation, they found that LNAPL redistribution is not straightforward, affecting the apparent thickness of the floating-free product in monitoring wells. However, their approach lacked imbibition/drainage cycles, limiting insights into dynamic redistribution. Gupta et al. (2019) conducted laboratory-scale 2D tank experiments to study the fate and transport of toluene in the unsaturated zone under water table fluctuations. They simulated slow, medium, and rapid fluctuations by decreasing the saturated zone by 5.0 cm over four, two, and one hour, respectively, but only considered one drainage event. Their findings highlighted that water table fluctuations significantly enhance bioremediation and strongly affect LNAPL fate and transport. Nevertheless, they recognized investigating subsurface heterogeneity as a potential direction for future research. Alazaiza et al., (2020) performed 1D laboratory experiments to examine drainage/imbibition cycles, varying the initial LNAPL volume and using image analysis to quantify residual fluid. Their results indicated that the initial fuel amount had minimal impact on fundamental LNAPL behavior. They used the Simplified Image Analysis Method (SIAM), which assumes a linear relationship between optical density and LNAPL/water saturation, achieving a 10% accuracy based on mass balance calculations. Koohbor et al. (2023) explored LNAPL redistribution under controlled water table fluctuations, focusing on gravitational and capillary interactions. Using a 2D tank with Time-Domain Reflectometers (TDR) and glass beads as the porous medium, their experiments were essentially 1D, as all drainage/imbibition processes occurred vertically, without heterogeneity, and under isothermal ambient conditions. Additionally, numerical simulations using COMSOL Multiphysics successfully reproduced their experimental findings, showing good agreement. Recently, Cavelan et al. (2024) conducted one of the most comprehensive studies on LNAPL behavior under groundwater level fluctuations and rainfall using a metric-scale lysimeter filled with homogeneous porous media, under isothermal conditions. Their work focused on transitions between free, residual, and trapped phases, demonstrating that water table fluctuations strongly influence LNAPL redistribution. These findings underscore the importance of incorporating real-world complexities into predictive models.

Heterogeneities in soil physical properties, particularly porosity and permeability, further complicate LNAPL distribution and redistribution during water table fluctuations. They also pose challenges for soil remediation techniques. Low-permeability zones, such as clay lenses or strata, divert fluid flow, introducing a significant horizontal component, whereas flow is mostly vertical in their absence. These low-permeability zones also serve as secondary pollution sources, as pollutants diffuse and back-diffuse into more permeable zones after remediation (Alamooti et al., 2025; Zuo et al., 2021).

Compared to studies on water table fluctuations, fewer investigations have focused on the effects of soil heterogeneities on LNAPL redistribution. Wipfler et al. (2004) examined LNAPL migration in stratified porous media under two heterogeneous configurations in a quasi-2D setup, where the permeability contrast between coarse and fine sand was approximately two. Their findings demonstrated that capillary barriers at permeability transition boundaries significantly impact lateral spreading and vertical migration. Zuo et al. (2021) explored the effect of heterogeneity on LNAPL migration, focusing on layered systems under rainfall-induced infiltration conditions. Their results showed that capillary barriers at fine-to-coarse layer interfaces control LNAPL redistribution, particularly under transient conditions.

However, to our best knowledge, neither study considered the impact of heterogeneity during water table fluctuations. Furthermore, all experiments were conducted at ambient laboratory temperature (20°C), whereas subsurface aquifer temperatures typically range from 9 to 12°C.

Temperature fluctuations can further influence LNAPL behavior by altering physicochemical properties. Higher temperatures reduce the LNAPL viscosity, increasing mobility while also lowering interfacial tension and promoting migration through interconnected pores. Temperature also enhances the volatility of certain hydrocarbon components, increasing the risk of vapor-phase migration and contamination (Imhoff et al., 1997; Kulkarni et al., 2017; McAlexander & Sihota, 2019). The physicochemical properties of DNAPLs and LNAPLs, such as viscosity, density, and interfacial tension, exhibit similar temperature-dependent trends. Higher temperatures generally reduce viscosity and interfacial tension, increasing fluid mobility (Philippe et al., 2020a). Additionally, temperature increases can enhance the volatility of light hydrocarbons, promoting vapor-phase migration. For instance, (Sleep & Ma, 1997) investigated temperature effects on PCE and Voltesso 35 (multicomponent branched alkane transformer oil, representative LNAPL), demonstrating that increasing the temperature from 20°C to 50°C reduced viscosity and residual saturation under dynamic conditions, thereby enhancing recovery processes. Similarly, Dou et al. (2022) examined NAPL redistribution under freeze-thaw cycles and found that temperature-induced capillary pressure can lead to significant fluid redistribution between different pore types. While their study focused on extreme temperature variations (-15°C to 20°C), their results highlight the critical role of temperature in fluid redistribution within porous media. In a comprehensive review, Cavelan et al. (2022) emphasized that climate-induced water table fluctuations and temperature variations can enhance LNAPL biodegradation, dissolution, and volatilization.

Most existing studies (Alazaiza et al., 2020; Cavelan et al., 2024; Kechavarzi et al., 2005; Koohbor et al., 2023; Yimsiri et al., 2018; Zuo et al., 2021) focus independently on either water table fluctuations or temperature effects, with none simultaneously investigating subsurface heterogeneities alongside these factors. Thus, the primary objective of this study is to investigate the combined effects of water table fluctuations and temperature variations on the redistribution of LNAPL in heterogeneous porous media. Specifically, this research introduces heterogeneities mimicking subsurface conditions, such as low-permeability lenses with a permeability contrast of 20. Laboratory experiments incorporating geophysical sensors and AI-based image analysis will provide insights into how dynamic environmental factors interact with subsurface structures to influence the fate and transport of LNAPL. The results will enhance predictive models of LNAPL behavior, facilitating the development of more effective remediation strategies for contaminated sites. By bridging the gap between controlled laboratory experiments and real-world conditions, this study aims to inform environmental management practices and improve decision-making for the remediation of LNAPL-contaminated subsurface environments.

MATERIALS AND METHODS

Materials

Diesel fuel provided by a TotalEnergies gas station with a density of 0.833 g cm^{-3} was used as the LNAPL. Tap water from the laboratory was used as an aqueous phase. Hydrophilic blue by FDS PRO® (Brilliant Blue FCF) and hydrophobic red Oil Red O by SigmaAldrich® dyes powder for water and LNAPL were used, respectively. These dyes were added at a concentration of 1.66 g L^{-1} of water and 0.55 g L^{-1} of LNAPL, respectively. The use of dyes enhanced the color contrast between the fluids, allowing them to be distinguished during image processing.

Interfacial tension of the representative LNAPL and aqueous phase under studied range of temperature were measured using the Drop Shape Analyzer Krüss ADVANCE DSA 100® using the pendant drop method. This method uses the Young Laplace equation to fit the interfacial tension (Berry et al., 2015). Rheological measurements were performed using rotational rheometer Thermo Scientific Haake Mars® III with cone-plate geometry. The procedures for both measurements and apparatus are well defined and explained in previous studies (Omirbekov et al. 2020; Baigadilov et al. 2025; Sabyrbay et al. 2025).

As a representative porous media, two different silica sand grain sizes were used: 1–1.25 mm (hereafter referred to as *coarse sand*) and 0.1–0.35 mm (hereafter referred to as *fine sand*) (see TABLES

Table 1). Porosity and permeability were obtained through 1D sand-packed column tests (30.0 cm length and 4.0 cm inner diameter). Procedure and methods used for the characterization of the sand properties are well described in previous works (Baigadilov et al. 2024; Baigadilov et al. 2025; Sabyrbay et al. 2025).

Two – dimensional tank setup

The 2D tank setup used throughout the study is schematically represented in Figure . The experimental setup also included a high-resolution camera NIKON D810® with NIKKOR LENS 105 (Nikon®) for the image acquisition during the process, a 300W floodlight (Broncolor®), and a peristaltic pump Watson Marlow® 530 U for the drainage-imbibition. The setup used for these experiments has proven to be consistent in previous studies on dense non-aqueous phase liquid flow and geophysical monitoring (Cochennec et al., 2022; Colombano et al., 2021a; Iravani et al., 2023; Koohbor et al., 2023; Philippe et al., 2020a).

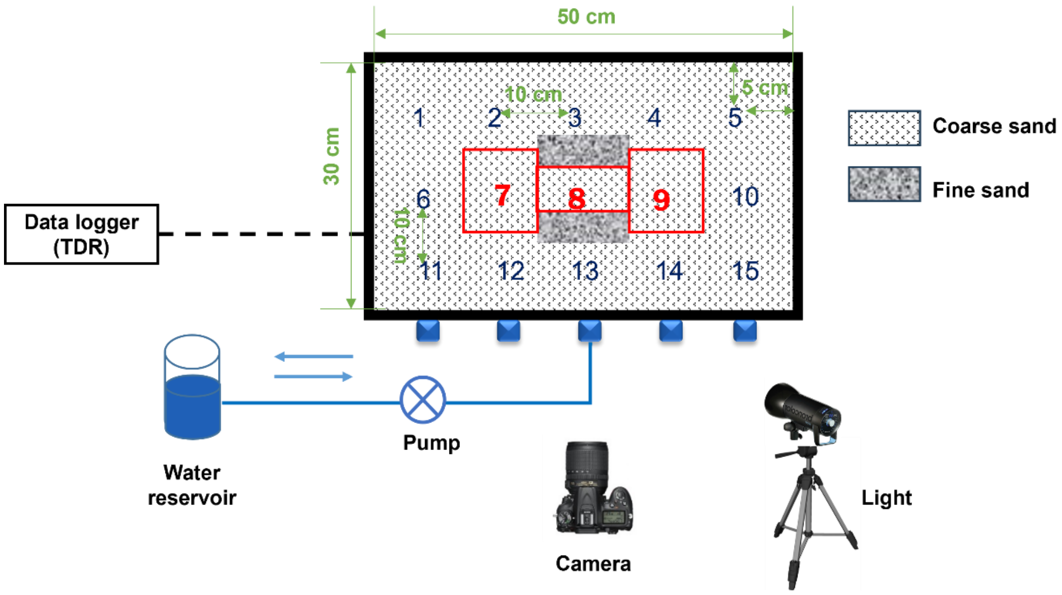

Figure 1. Schematical representation of the experimental setup. The numbers indicate the locations of the time domain reflectometry (TDR) probes. The red boxes highlight the areas of interest.

Two-dimensional tank was made of polyvinylidene difluoride (PVDF) with the following dimensions: length = 50.0 cm, height = 30.0 cm, and width = 8.5 cm. It was equipped on the back side with a network of 15 Time Domain Reflectometry (TDR) 5TE probes provided by METER GROUP® connected to Campbell® CR-1000 datalogger. The TDRs measured the relative permittivity with an accuracy of 0.1 permittivity value, and the temperature of the medium inside the 2D tank with an accuracy of 1°C. Using TDR probes, the phase saturation at different points within the 2D tank can be obtained, allowing for integrated methodology on saturation results derived from three-phase flow imaging. The tank was also equipped with five nozzles (internal diameter 3.125 cm) from the bottom, which allows the pump/inject operations to be performed on the internal reservoir. The front side of the 2D tank was made of 1 cm thick glass, allowing for observation and photography during the imbibition-drainage processes. There were double-glazing panels on the front side and an internal double wall on the back side, which allowed for the circulation of a thermostated fluid to regulate the temperature of the 2D tank, allowing experiments under isothermal conditions. The temperature adjustment was performed using a thermostatic bath (LAUDA® model ECO RE420), filled with water.

One of the main advantages of the 2D tank is its ability to better mimic aquifer conditions, such as heterogeneity, by introducing low-permeability lenses inside the box. The 2D tank setup was heterogeneously packed with coarse sand as the main porous medium, with two low-permeability lenses, each 10.0 cm wide and 5.0 cm high, made of fine sand and placed in the middle. The procedure for packing the system was as follows.

Experimental procedure

The bottom of the tank was incrementally wet-packed with 2–3 cm of coarse sand, without any additional weights for the compaction, followed by the placement of a lower fine sand lens at one-third of the tank height. First, water was introduced from the bottom of the tank at a very low flow rate to reach a height of 2–3 cm, minimizing the entrapment of air. Then, sand was added from the top. Two vertical plates were inserted to fix the width of the fine lenses and not intrude on the coarse sand matrix, thereby separating the low- and high-permeability zones. Plates were then removed from the top of the 2D tank. The wet-packing process continued until the top third of the tank, where the second fine sand lens was created, then the final layer of coarse sand was placed to completely fill the tank.

To better mimic realistic conditions, the entire system was initially water-saturated and then drained to a height of 10.0 cm from the bottom (one-third of the 2D tank height). This process left residual water in the upper two-thirds of the tank, including the top fine sand lens of low-permeability media. To mimic a spill scenario, LNAPL was then infiltrated at a rate of

6.2 mL min^{-1}, for 70 min in total from the top center of the 2D tank, and a total of 1400 mL of LNAPL was injected. Given that the mean temperature of the subsurface aquifer ranges from 9 to 12°C (IPCC., 2021), the thermostated bath was adjusted to maintain an approximate temperature of 10°C inside the 2D tank during LNAPL infiltration.

After LNAPL infiltration, an equilibrium period of 17 h was maintained before starting the drainage-imbibition experiments. Drainage and imbibition events were conducted by pumping in and injecting water from the bottom of the 2D tank using a peristaltic pump at a constant flow rate of 3.4 mL min^{-1}. Each drainage-imbibition event lasted at least 7 h, during which images were taken, and relative permittivity values were measured. The imbibition process began and continued until the LNAPL level (e. g.) reached the top of the tank, followed by drainage until the LNAPL level reached two-thirds of the tank. Two temperature settings (10°C and 20°C) were tested, with at least three drainage-imbibition cycles performed for each temperature.

Data curation and interpretation

Image treatment and analysis

Images and TDR values were captured and recorded simultaneously, facilitating post-processing. Focusing on the capillary fringe zone, with the three phases mixed most of the time, we have defined three areas of interest (AOI) to analyze the images: (1) the area between the two low-permeable lenses designated the "sandwiched zone" and positioned near the zone of influence of TDR 8 (Figure); (2) an area situated near the zone of influence of TDR 7 and (3) TDR 9 in the "coarse sand matrix". The dimensions of all the images are kept identical and manually cropped for each image.

The image interpretation procedure involved using an AI model on the Biodock® (*Biodock*, 2024; Williams et al., 2025) platform to identify air bubbles trapped within the designated area of interest. The modelling workflow consisted of data preparation, object labelling, model training, evaluation, and validation. First, we prepared the input data by manually cropping each image. Then, we classified the photos based on the intended analysis; for our study, the most suitable classification type was "object". Labelling was performed by dividing each image into smaller tiles, and within each tile, the object (air bubble) was identified. Dividing the image into smaller tiles improved the accuracy of air bubble detection.

Next, the model was trained by labelling air bubbles across multiple images and then tested. The final output of the model was the total area of detected air bubbles within an image. Since the total area of each image was known, we calculated the pore space per image by multiplying this value by the porosity. Finally, air saturation was determined by dividing the total detected bubble area by the total pore space area.

A script written using OpenCV (Bradski & Kaehler, 2008), a computer vision library, was used to analyze the saturation by water and LNAPL based on red and blue color intensities. The procedure for analysing water and LNAPL saturation involved creating blue and red masks per image, thanks to the hydrophilic and hydrophobic dyes used for the aqueous water phase and LNAPL during the experiments. Original images were converted to 8-bit images in a suitable format for OpenCV. Thresholds were set for the hue, saturation, and value, creating masks for the red and blue colors. Subsequently, by defining the areas corresponding to each mask and dividing them by the total area, we obtained saturation by each color. We created two masks for the red color to better stress out the red-colored areas.

Next, the values obtained from OpenCV were normalized. The air saturation value obtained from the AI model was considered as a constant value, and the saturation of LNAPL and water are derived through the normalization. Applying the saturation sum rule (which equals one), we normalize the values using Eq. (1):

$$\boldsymbol{S_d} = \frac{\boldsymbol{S_{red}}}{[(\boldsymbol{1} - \boldsymbol{S_{air}}) \times (\boldsymbol{S_{red}} + \boldsymbol{S_{blue}})]} \tag{1}$$

where S_d (-) is the saturation of the LNAPL phase and S_{red} (-) is the saturation of red color obtained from the OpenCV model, S_{air} (-) saturation of air obtained from Biodock, S_{blue} (-) is the saturation of blue color obtained from OpenCV. Water saturation is calculated using the same equation but with the replacement of S_{red} by S_{blue}. Example of outcome images from the image treatment are presented in Figure S4 and Figure S5 in the supplementary materials. The result of this analysis is presented in the following sections.

In this regard it is important to mention the role of image quality on the phase detection accuracy. Here, we have used output images with 300 dpi resolution. Given the size of the picture, the scale is one pixel = 0.084 mm. Although it is sufficient to clearly delineate a cluster of water/LNAPL, some very small air bubbles might not be clearly seen.

Sensitivity analysis of the hue–saturation–value (HSV) threshold using the representative masks under different threshold settings (Figure S6) as well as the error margins and statistical summaries (mean, STD, and 95% confidence intervals with lower and upper bounds) (Table S3) are reported in the supplementary materials. These intervals quantify the variability introduced by reasonable HSV threshold selections and serve as explicit uncertainty bounds for the image-processing results. Importantly, the observed trends and interpretations are unchanged when these uncertainties are propagated. Regarding continuity of saturation between successive cycles, the pairwise differences are generally within the reported STDs (and their 95% CIs), indicating that any small offsets are comparable to measurement uncertainty and do not alter the conclusions.

TDR data treatment

Permittivity data, as well as temperature, are obtained from the TDRs located inside the 2D tank. Before starting the experiments, reference TDR permittivity values were obtained for the porous medium and pure phase fluids at different temperatures. The measurements for pure phase fluids were taken inside the 2D tank without porous media. The permittivity was measured over a temperature range of 10°C to 30°C for 24 hours. Obtained pure phase permittivity results were applied accordingly for each temperature range. The Complex Refractive Index Model (CRIM) (Brovelli & Cassiani, 2008) was used to calculate the saturation from the permittivity values (Eq. (2)). In this equation, we initially have three unknowns related to the saturation of the three phases; hence, we applied the air saturation values obtained from the image treatment on Biodock AI platform (explained further) as a reference.

$$\sqrt{\varepsilon} = \phi\left(S_a\sqrt{\varepsilon_a} + S_w\sqrt{\varepsilon_w} + S_d\sqrt{\varepsilon_d}\right) + (1-\phi)\sqrt{\varepsilon_{solid}} \quad (2)$$

where ε_w, ε_d and ε_a are relative permittivities of the water, LNAPL and air phases, respectively (-), ε_{soild} bulk relative permittivity of the sand material, e.g., silica (-), ϕ is porosity of the porous medium (-), S_w, S_d and S_a are saturation of the water (-), LNAPL (-) and air (-) respectively, ε is the measured relative permittivity during the experiments (-). To account for temperature effects on fluid properties, the phase permittivity values used in the CRIM equation were adjusted based on the measured temperature for each experimental stage, using the relationships shown in Table 2. The zone of influence of TDR probe reported by the manufacturer for the aqueous phase (air-water system) is 5.0 cm. However, the zone of influence of TDRs has been experimentally detected at around 2.0 mm of the probe for the NAPL phase (Figure 2 in (Colombano et al., 2021)). In this work we computed saturations from the real part of the bulk permittivity (ε′) using CRIM; we did not invert for the imaginary part (ε″) or frequency dispersion (Ajo-Franklin et al. 2004; Colombano et al. 2021).

RESULTS

Permittivity responses during LNAPL infiltration

The redistribution of LNAPL is a complex process influenced by several factors, including subsurface conditions, compounds in the LNAPL mixture and the amount of fluid released (Cavelan et al., 2022; Dou et al., 2022; Gupta et al., 2019; Rivett et al., 2014). However, it is preceded by infiltration through the unsaturated zone followed by LNAPL distribution on the water table. Therefore, our study begins by describing the primary release of LNAPL into the studied system before cycles of imbibition and drainage. This represents a more realistic initial condition for the experiments.

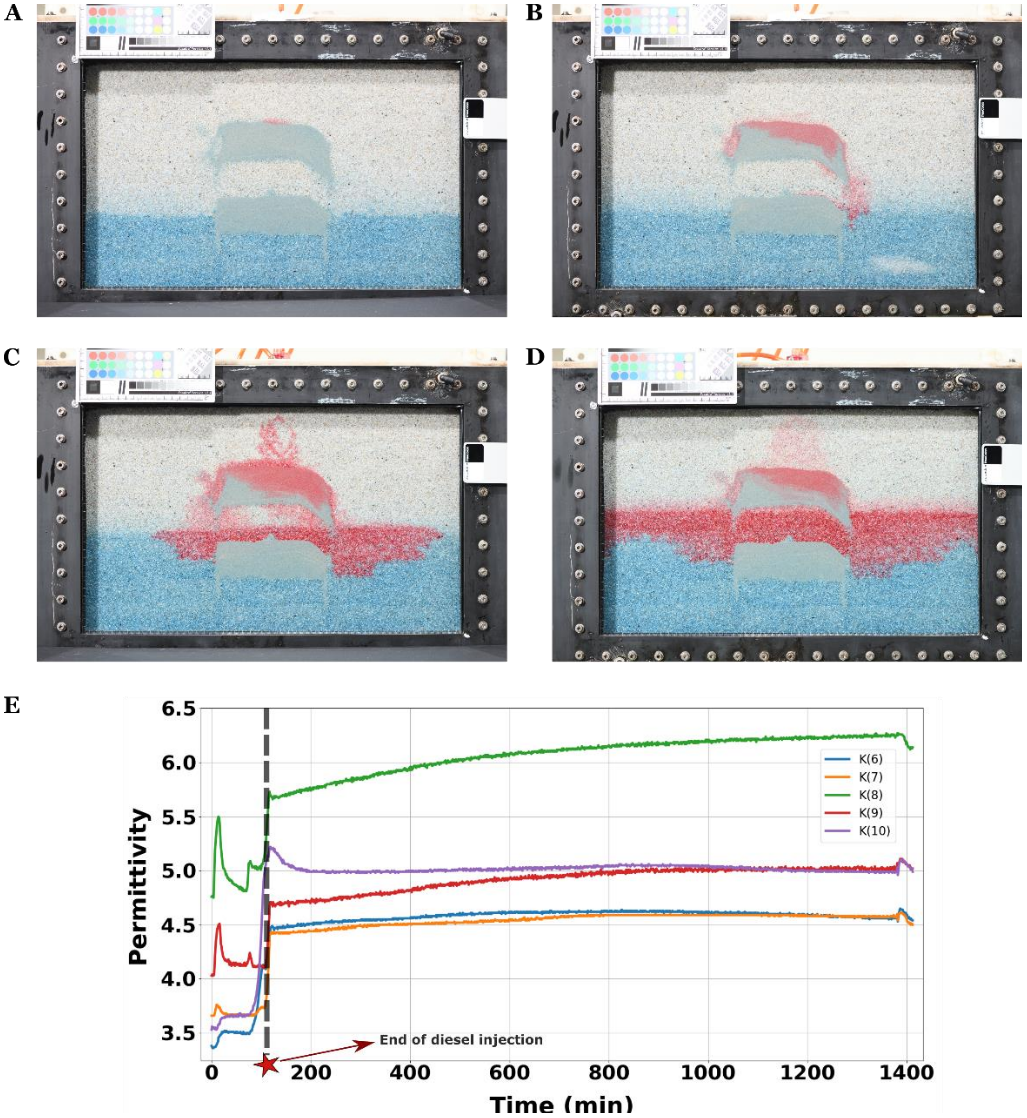

Figure 2. LNAPL infiltration (red color - LNAPL, blue color - water): (A) at the beginning, (B) after 25 minutes, (C) after 95 minutes, (D) 1400 minutes, and (E) permittivity values during LNAPL infiltration.

The infiltration of LNAPL into the 2D sand-packed tank, partially saturated with water, exhibited distinct behaviors influenced by the varying permeability zones within the system.

Upon the introduction of the LNAPL at the top center of the tank, the initial accumulation was observed over the first low-permeability lens. Further, LNAPL partially infiltrated the low-permeability zone due to the relatively low entry pressure, influenced by the presence of air. Despite entering the low-permeability zone, the LNAPL did not fully penetrate this region, instead flowing along the top boundary of the lens, where it could bypass the barrier and move laterally toward the water table, as illustrated in Figure A and B.

As the LNAPL continued to migrate vertically downward, it encountered the underlying lower lens, which was fully saturated with water. The high entry pressure associated with the water-saturated lens prevented further infiltration of LNAPL into this region. Instead, the LNAPL continued to spread across the tank, driven by both gravitational forces and viscous effects, pushing a portion of the water in the central region of the tank (Figure C and D).

Notably, the LNAPL exhibited a slow, sliding motion along the water surface, especially at the two extremities of the 2D tank. In these areas, the LNAPL floated on the water's surface without displacing any significant volume of water beneath it. This behavior is consistent with the expected dynamics of LNAPL infiltration in aquifers (Tomlinson et al., 2017), where the interaction between the LNAPL, water, and the porous medium results in complex flow patterns, particularly when contrasting permeabilities and varying entry pressures are present.

Figure (E) demonstrates the permittivity values of TDR 6 – 10 in the middle of the 2D tank during the infiltration process. Corresponding images of the 2D tank during the LNAPL infiltration are illustrated in Figure (A - D), where (A) represents the beginning, (B) shows the state after 25 min, (C) after 95 min, and (D) after 1400 min. From Figure (E) one can observe an increase in permittivity values at the beginning of LNAPL injection for all five sensors. This increase is attributed to the rising water content in the TDR influence zone, caused by the displacement and redistribution of water and air as LNAPL infiltrated. Displacement of trapped air by LNAPL also likely contributed, since replacing low-permittivity air with higher-permittivity fluids (water and LNAPL) increases the bulk permittivity. However, the slope is sharper for TDR 8 and 9, located in the middle and right side of the tank. This may be explained by LNAPL being injected from the top of the tank, which caused water to migrate into the influence zone of these sensors. Furthermore, LNAPL appeared more rapidly in this area compared to the other side of the tank. After 25 min of injection, misalignment in LNAPL spreading was observed (Figure (B)), and injection was stopped. After 40 min following the first injection, it was restarted with an adjusted injection point to obtain a more even LNAPL distribution. The total LNAPL injection flow rate was kept constant throughout the experiments. Upon restarting the injection, Figure (E) shows another increase in permittivity values, but this time with a steeper slope for the TDRs 6 and 10, indicating that LNAPL displaced water into their influence zones. Furthermore, at 110 min, the injection was stopped, and the permittivity values began to stabilize. By 1400 min (around one day) after the initial injection, permittivity values remained stable or showed a slight increase (as seen for TDR 8), likely due to the balancing of capillary, gravity, and viscous forces. After this stabilization period where all phases are in equilibrium state, the first imbibition began.

LNAPL saturation profiles in zone of TDR9

The zone near TDR 9 is in a matrix of coarse sand and represents the LNAPL distribution in a relatively homogeneous environment. This is why we selected this zone to evaluate the impact of drainage–imbibition cycles on LNAPL distribution. Since TDR 9 is at the same distance from TDR 8 as TDR 7, similar behavior is expected. Figure 3 illustrates the

LNAPL saturation profiles for the zone near TDR 9 at 10°C as a function of normalized time (image acquisition time divided by the total experiment duration). Subfigures A and C show image-analysis-based saturation values, whereas B and D correspond to TDR-based results. Four imbibition drainage cycles are presented, distinguished by different shades of colors and markers.

As shown in Figure 3 (A, B) both image-based and TDR-based imbibition profiles follows the same sequence, characterized by a sharp drop in saturation after a normalized time of 0.2–0.3. The image-derived profiles reach zero or near-zero values toward the end of imbibition, reflecting the displacement of LNAPL from the analyzed area of interest (AOI), as visually confirmed across the full images’ series. In contrast, the TDR-based profiles reached the lowest value at the midpoint of normalized time.

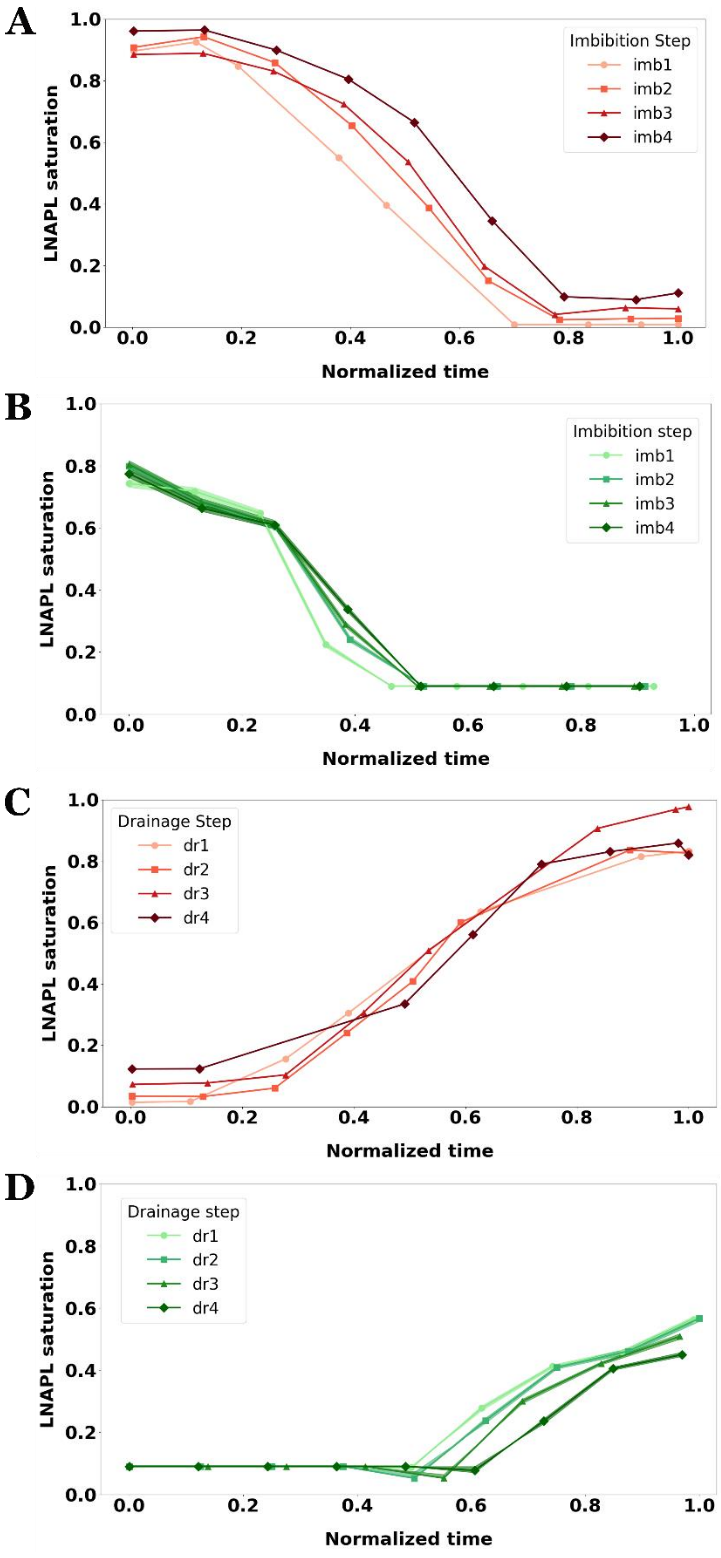

Figure 3. LNAPL saturation profiles as a function of normalized time (the time in minutes when the image was taken divided by the total number of minutes) at TDR9 zone for 10°C experiments: A) imbibition based on the image, B) imbibition based on TDR, C) drainage based on the image, D) drainage based on TDR

Notably, image analysis-based saturation values were consistently higher than TDR. This discrepancy is primarily attributed to the different spatial scales of the two methods: the AOI for images is significantly larger than the TDR probe's limited zone of sensitivity for the NAPL phase (2.0 mm). As the water level rose, the water-LNAPL interface bypassed the influence zone of TDR 9, resulting in a lower detected saturation, while LNAPL remained visible within the broader AOI of the images.

The minor increase in image-based saturation values at normalized times 0–0.2 likely reflects the presence of air at the beginning of imbibition. As imbibition progressed, the air was displaced by LNAPL, leading to higher LNAPL saturation in the images. Meanwhile, the TDR profile did not capture this behavior because the LNAPL-air interface was located above the probe’s zone of influence. Cycle-to-cycle differences in the Figure 3 (A, B) residual LNAPL saturation at the normalized times 0.8-1.0 indicate hysteresis, as prior cycles influenced subsequent distributions through wetting/non-wetting events, thereby altering residual saturation.

Drainage results Figure 3 (C, D) further highlight discrepancies of AOI of image- and TDR- based values. While TDR-based saturation profile (D) remained relatively stable until a normalized time of 0.5–0.6, before gradually rising, image-based profiles detected saturation increases earlier at a normalized time of 0.2–0.3. Both methods showed a gradual decrease in the saturation rise at later steps. Moreover, Figure 3 (D) shows lower endpoint saturations for cycles 3 and 4 compared to cycles 1 and 2, attributed to LNAPL entrapment in the upper part of the tank within previously unsaturated zones. Image-based saturation profiles demonstrated similar trends except for the third drainage cycle, where reduced image resolution resulted in an overestimation of LNAPL saturation.

Discrepancies between Figure 3 (C) and Figure 3 (D) were consistent with the earlier-mentioned variation in the sensitivity of the TDR to LNAPL compared to water. Images centered over TDR 9 (Figure) taken during the experiments clearly showed the absence of water in the studied zone. Readers are encouraged to refer to Figure S1 in the supplementary materials, which provides the full-view images of the 2D tank, highlighting the final step of each imbibition (*i(n)*) and drainage (*dr(n)*). TDR 7, symmetrically positioned relative to TDR 9 on the opposite side of the tank, demonstrated similar saturation profiles (Figure S2).

LNAPL saturation profiles in zone of TDR8

Figure presents the LNAPL saturation profiles derived from image analysis (A and C) and permittivity values (B and D) at 10°C as a function of normalized time for the region centered on TDR 8. This TDR was placed in the zone between the two low-permeability lenses (the "sandwiched zone"), which is suitable for evaluating the impact of heterogeneity on LNAPL distribution. During imbibition (Figure , A and B) saturation decreased progressively after the first three measurement points, as the water level rose in the studied zone and then stabilized normalized time of 0.5–0.6. Both profiles follow the same sequence, with LNAPL entrapment increasing with each cycle. Higher saturation values following imbibition indicated hysteresis, caused by progressive wettability alteration and accumulation above the low-permeable lens as discussed by (Kong & Shao, 2023; Radke et al., 1992); full-view tank images support this interpretation (Figure S1).

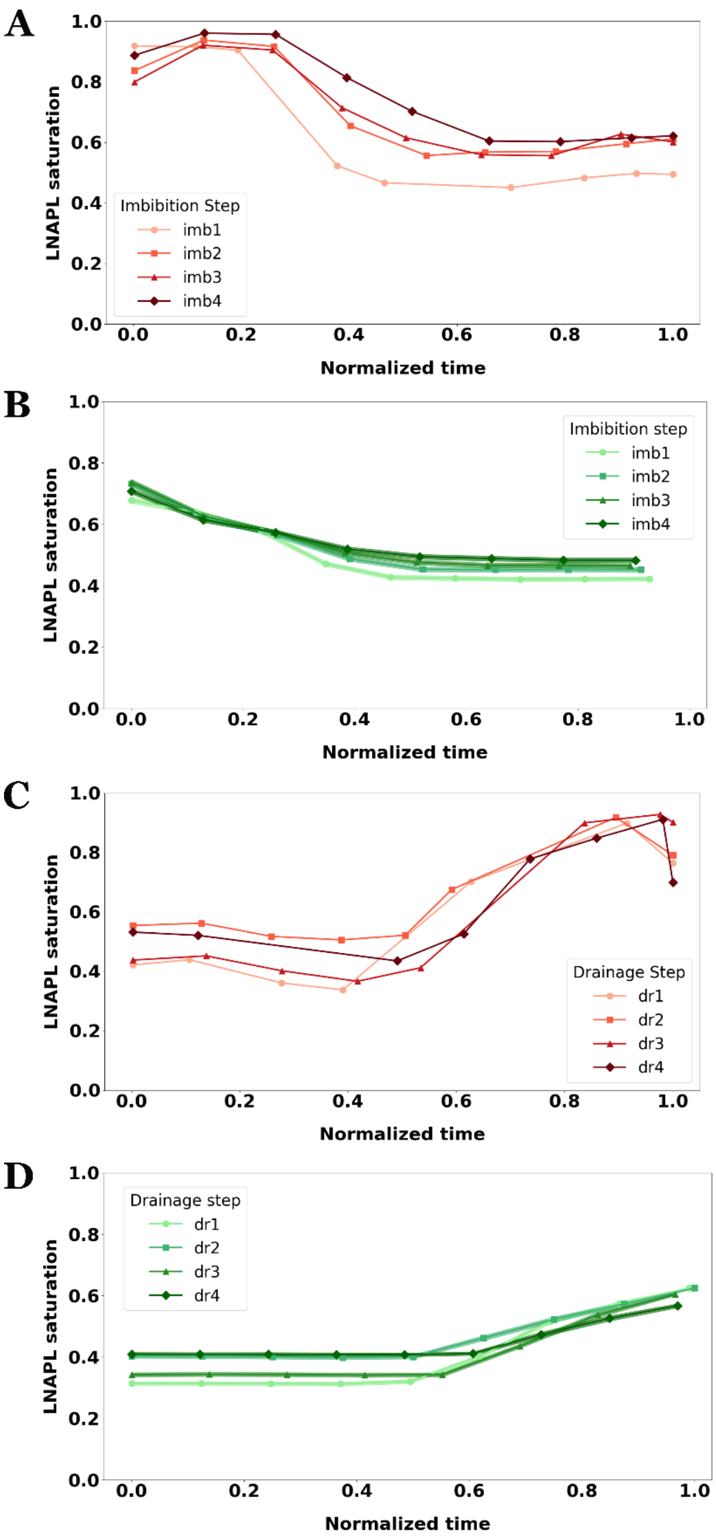

Figure 4. LNAPL saturation at sandwiched zone for 10°C experiments as a function of normalized time (time in minutes at which image was taken divided to the total time in minutes): A) imbibition based on the image, B) imbibition based on TDR 8, C) drainage based on the image, D) drainage based on TDR 8

In Figure A, a noticeable "jump" in saturation occurs at the start of imbibition cycles 2 to 4. This behavior corresponds to a higher air content in these cycles (air saturation was 17%, 21%, and 12%) relative to cycle 1 (8.5%) due to lower air-LNAPL interface. Following a rise in water level between two measurement points, air was displaced by LNAPL, thereby generating the observed jump in image analysis-based profiles. This jump is not visible in cycle 1 because initially higher LNAPL saturation limited early air displacement. This effect is also absent in TDR-based profiles (panel B) because, at that time, the air-LNAPL interface did not reach the probe's sensitivity zone.

In addition to the temporal behavior described above, systematic discrepancies observed from Figure 4 is that across cycles saturation values obtained from images (A) are consistently higher than permittivity-based results (B). Two mechanisms likely to contribute: (i) a wall effect, as previously described by Mehta & Hawley (1969), arising from permeability differences near the TDR probe and the glass window; a locally higher permeability zone may be present (within the AOI), facilitating fluid flow; (ii) phase-dependent sensitivity of the TDR probe. For the NAPL, the TDR sensitivity zone might extend 2.0 mm, whereas for water, it extends 5.0 cm. The distance between TDR 8 and the low-permeable lenses is 2.5 cm to the bottom and 1.5 cm to the top, meaning that trapped water within the lenses could affect the permittivity response. Consequently, as the water level rose, the water-LNAPL interface often remained outside TDR8's zone of influence, and LNAPL was still visible within the broader AOI of images and led to systematically higher images-derived values. While we assume the wall effect to be a secondary factor, it is a known artifact in 2D tank studies that can create preferential flow paths along the glass interface. This may partly explain why image analysis records higher LNAPL saturation compared to the TDR probe embedded within the sand matrix.

During drainage (Figure C and D), both methods showed LNAPL saturation increasing from normalized time of 0.5. The rise in image-based profiles (C) is sharper than in TDR-based profiles, consistent with larger AOI in the images and limitation of TDR sensitivity zone (see section 2.3). In images LNAPL is detected earlier, whereas TDR probes record a delayed response. Thus, the drop in LNAPL saturation at the end of drainage reflects that the air-LNAPL interface did not reach TDR8's zone of influence. At the last drainage measurement points for cycles one to four, air saturation values based on image analysis were 25%, 22%, 11%, and 32%, respectively (Table S2) consistent with interface positions observed in images (Figure S1).

Figure (D) also demonstrates that drainage cycles 1 and 3 have similar behavior, as do cycles 2 and 4. This pattern likely reflects differences in the delay times between imbibition and subsequent drainage: intervals before drainage 1 and 3 were longer than those before drainage 2 and 4. A similar trend is observed in the image-based profiles in Figure 4 (C). At their endpoints, a drop in LNAPL saturation is visible, attributable to a lower position of LNAPL-air interface and a larger air presence within the AOI.

Phases behavior as a function of temperature

Table 3 represents the measured values of viscosity of LNAPL and interfacial tension of LNAPL-water in the studied temperature range. Although temperature is inversely proportional to both viscosity and interfacial tension, in the studied temperature range for LNAPL as a pollutant, viscous forces were dominant rather than capillary.

Table 2 shows the dependence of permittivity for pure phases of air, LNAPL, and water on temperature. The measurements were taken inside the 2D tank without porous media, over a temperature range of 10°C to 30°C for 24 h. The permittivity trend for each phase aligns well with the literature (Iravani et al., 2020; Rosenbaum et al., 2011), indicating that while the permittivity of the water phase decreases with temperature, an inverse trend was observed to LNAPL and air. This is attributed to the permittivity responses to the polar non-polar fluids (Iravani et al., 2020; Riley, 2013). Some noisy data were observed for the water phase, which may be related to the conditions under which the measurements were taken, as they were conducted immediately after the set of experiments (Figure S3). This could have resulted in changes to the wettability of the TDR sensors, explaining the fluctuations. However, the general trend is logical and agrees well with literature.

Figure displays the 2D tank images after imbibition 4 (i4) and drainage 4 (dr4) as well as imbibition 5 (i5) and drainage 5 (dr5) (temperature increased from 10 to 20°C after the dr4). Visually, a negligible difference in LNAPL distribution was observed after imbibition 4 and 5. In both images, the lateral extension of trapped LNAPL after imbibition could be observed from two sides of the low-permeable lenses.

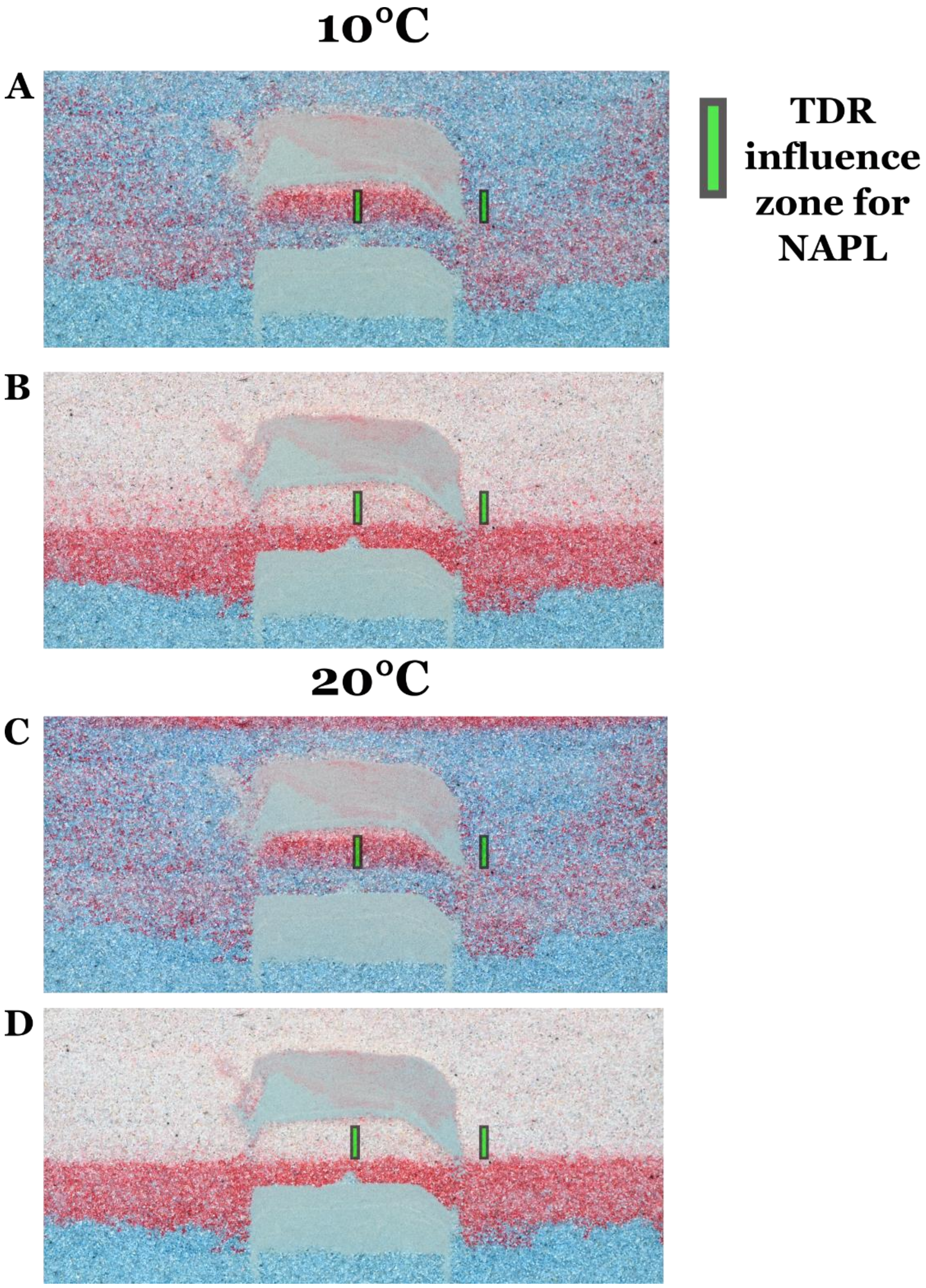

Figure 5. 2D tank after temperature changes. Images after A) imbibition 4, B) drainage 4, C) imbibition 5, and D) drainage 5 are displayed with the influence zones of the TDR 8 and 9 in light green rectangles. Temperature increased from 10°C to 20°C after drainage 4.

Conversely, after drainage, a noticeable reduction in residual LNAPL trapped above the low-permeable lenses was observed at 20°C compared to 10°C. As illustrated in Figure, following the drainage cycle 5, the residual LNAPL present within the vadose zone was significantly diminished.

To support our qualitative analysis, Figure compares saturation profiles based on the permittivity values of TDR 9 (A) and the image treatment (B) for drainage 4 and drainage 5. For both profiles, it is evident that the saturation values are higher in the case of drainage 5. The image-based profiles register increase earlier and report higher LNAPL saturation over the interval than TDR-based profiles. As previously discussed, the higher saturation values in the image-based profile are due to the larger AOI compared to the TDR's zone of influence.

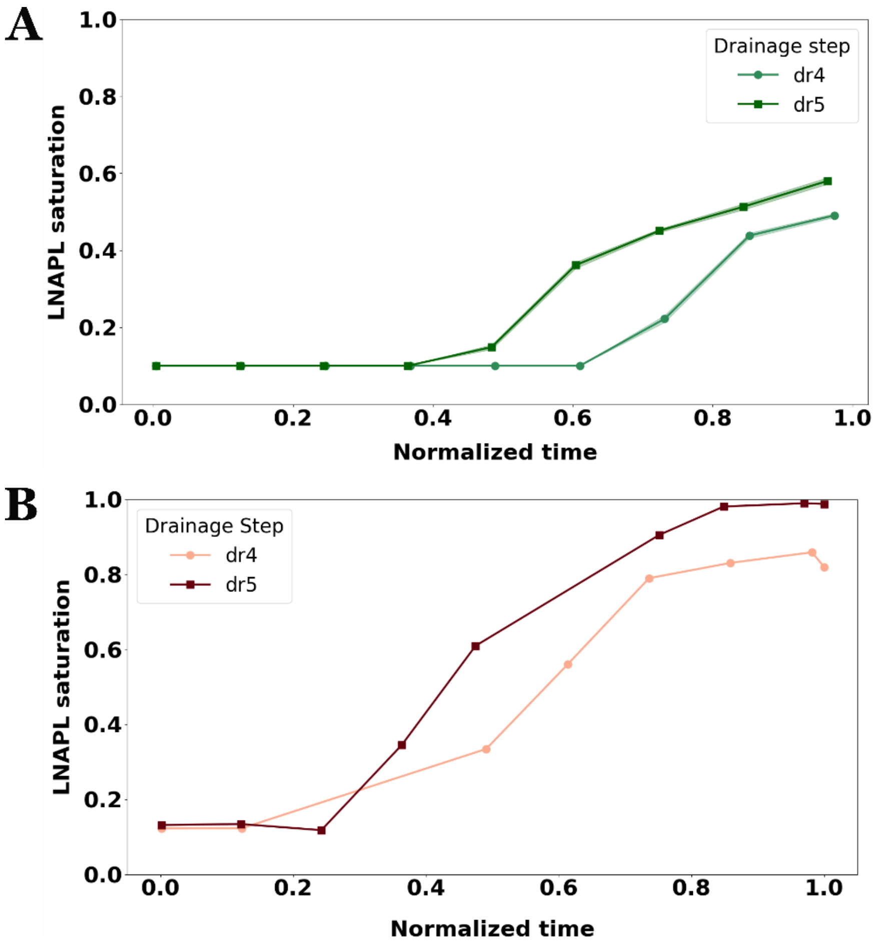

Figure 6. Saturation profiles for TDR9 zone before (drainage 4) and after (drainage 5) temperature change A) based on permittivity values, B) based on image analysis

DISCUSSION

Impact of heterogeneity on LNAPL entrapment

Across cycles, the homogeneous domain showed an earlier and sharper saturation change rates during the imbibition and more smooth and uniform increase in saturation during drainage. In contrast, a sandwich zone shows delayed change and consistently higher residual LNAPL. This behavior highlights the presence of capillary barriers on the interface of the low-coarse sand. Pore throat size in the permeability boundaries is less, and capillary entry pressure is higher, thus movement of the fluids in the boundaries is limited until threshold pressure is surpassed (Blunt, 2016).

Our studies are in well alignment with previous 2-D tank studies in heterogeneous media. Zuo et al. (2021) in their study on layered media have reported lateral spreading and accumulation at fine-coarse interface that acted as capillary barriers. They also reported a slower movement in fine layers and a higher displacement rate in coarse sand. These phenomena are consistent with capillary dominated flow and heterogeneity-controlled redistribution. Similar observations were reported by Zhao et al. (2024) on the impact of lenses on LNAPL migration. In their study they have tested three porous media structures: homogeneous, low permeable lens and high permeable lens. They showed that higher capillary entry pressure near low permeable lens enhanced lateral movement and local entrapment. The homogeneous zone in their study has also demonstrated rapid and smooth saturation change, consistent with our observations.

Immiscible displacement in porous media is governed by capillary, viscous and gravity forces and the dominance or intercourse can be distinguished through non dimensional numbers: capillary number *Ca* (interplay of the viscous and capillary forces), viscosity ratio *M* (viscosity relations of invading and displaced fluids). On a macroscopic level, gravity forces predominate, while phenomena occurring at the pore scale are influenced by viscous and capillary forces. We assess the dominance through the equations below:

$$Ca = \frac{\mu_{invading} U}{\sigma} \tag{3}$$

$$M = \frac{\mu_{invading}}{\mu_{displaced}} \tag{4}$$

where, $\mu_{invading}$ and $\mu_{displaced}$ are the viscosities (mPa·s) of the invading and displaced fluids respectively, *U* is Darcy velocity ($m \cdot s^{-1}$) and σ is the interfacial tension ($mN \cdot m^{-1}$) of the invading and displaced fluid. Dimensionless numbers of our study are presented in the Table 2. During drainage, the conditions of $Ca_{dr} << 10^{-5}$ and $M > 1$ correspond to the viscous force favorable displacement, but with capillary-dominated regime at the pore scale (Lenormand et al., 1983). Meaning that menisci penetrate the pore throat intermittently via Haines jumps (Albers, 2014; Blunt, 2016) and create limited connectivity of the phase and subsequently impacting the residual saturation. Whereas during the imbibition of $Ca_{imb} << 10^{-5}$ and $M < 1$ aligning with the classification of capillary-controlled flow proposed by Lenormand. At the pore scale wetting films promote snap-off mechanisms and led to the entrapment hysteresis.

Hysteresis and effect of wettability alteration

Hysteretic behavior in LNAPL saturation was observed through image and TDR analyses, with increased LNAPL entrapment in the capillary fringe after each imbibition cycle. This is attributed to wettability alteration from initially water-wet to mixed-wet conditions, consistent with findings by Anderson, (1986), Kong & Shao, (2023) and Radke et al., (1992). Initially, the silica sand was fully water-saturated and subsequently drained before LNAPL infiltration. At the pore scale, a thin water film initially coated the sand surfaces. Repeated exposure to LNAPL led to the rupture of this film due to the adsorption of polar hydrocarbons, promoting a shift in wettability (Anderson, 1986). Earlier work by Radke et al. (1992) have reported similar phenomenon, where hydrocarbon presence induced mixed-wet conditions in silica sand. Among the three types of pores—small, large, and intermediate—they observed asphaltene adsorption on sand surfaces covered by a thin aqueous phase film. In small pores, only the aqueous phase was present, whereas in large pores, the water film covering the sand surface was thick. In intermediate-sized pores, a thin water film was maintained. They proposed that in pore walls where oil was present, water films were disrupted, leading to asphaltene adsorption and oil-wet behavior. Kong & Shao (2023) has also observed in their study of the impact of sand grain size on LNAPL infiltration in the Miller sandbox. They tested three grain size ranges and developed a model describing wettability alteration over time. For example, they observed that for fine and medium sands, which were initially water-wet, wettability changed in four stages, eventually becoming oil-wet due to prolonged LNAPL presence.

Impact of temperature variation on LNAPL mobility

Both viscosity and IFT are temperature dependent parameters, but in the studied range of temperature impact of viscosity variation was higher than IFT. In porous media the phase mobility is defined as

$$\lambda = \frac{k_r}{\mu} \tag{5}$$

where λ denotes the fluid mobility, μ is the viscosity (mPa·s) of the given fluid and k_r is the relative permeability of the given fluid. Hence, as given in

Table 3 elevated temperature resulted in viscosity drop enhancing the mobility. In contrast, capillary entry pressures, dominating the imbibition, depend mainly on the contact angle and interfacial tension, which changed around 3% over this range. Therefore, the capillary number, Ca was not largely affected and increased mobility of the LNAPL by elevated temperature had an influence on drainage rather than imbibition. Consequently, saturation profile after drainage 5 showed lower values compared to drainage 4 and enhanced downward redistribution at higher temperature.

It has been reported that viscosity of LNAPL decreases significantly as the temperature rises (Daučík et al., 2008; Niţă et al., 2021). Niţă et al., 2021 have reported the change of LNAPL viscosity from 4.45 mPa·s to 3.41 mPa·s over a temperature change of 10 degrees (Figure 1 in Niţă et al. (2021)). It reflected the LNAPL displacement after drainage. Adjacent temperature change increased the LNAPL mobility and drainage profiles indicated lower

LNAPL saturation. Additionally, based on Sleep and Ma 1997 viscosity drop up to 41% can be resulted by temperature increase from 12 to 20 degrees. Our results are also in good alignment with controlled experiments reported by Philippe et al., 2020b. They observed a strong decrease in viscosity of all four fluids in their study (ethanol, canola oil, coal tar and water) in response to the temperature variation from 12°C to 50°C. They have also reported that mobility rose with temperature due to both increased relative permeability and decline in viscosity leading to lower residual saturation of DNAPL at elevated temperature, S_{ro} 16% down to 6%. Taken together, these studies and our findings highlight that temperature-driven viscosity reduction directly governs NAPL redistribution, particularly under drainage conditions

CONCLUSIONS

To investigate the impact of groundwater table fluctuation and temperature on LNAPL redistribution in heterogeneous porous media, a series of experiments were conducted in a 2D tank packed with silica sand and diesel fuel as the representative LNAPL. Two different techniques (TDR and imaging) were used to analyze the three-phase flow behavior during the drainage and imbibition cycles. Bulk dielectric permittivity values were measured using TDR probes and converted to saturation values according to the CRIM equation. High-resolution images were analyzed using the AI-based Biodock platform and OpenCV in Python. Saturation profiles by LNAPL were built based on TDR measurements and image analysis. Because inability of TDR to differentiate air from LNAPL required us to use air saturation values from image analysis as an input for the CRIM equation, making this an integrated workflow rather than two independent measurements.

The experiments specifically focused on the multiphase flow, however, the dissolution and volatilization mechanisms at both the field and laboratory scales have not been investigated. Both might change the LNAPL composition throughout the experiments, e.g., with increasing relative concentration of longer alkanes and by altering the aromatic content. Here total petroleum hydrocarbons including both alkanes and aromatic compounds are considered to span C10-C40 by carbon number. It would be also interesting to investigate the behavior of the aged pollutant and/or mixture of the several pollutants as in a real-world scenario. Additionally, the present study was conducted under controlled conditions, with a constant flow rate and a constant capillary number. However, in practical application, the rate of oscillation and the rate of temperature variation may fluctuate for water table fluctuation events, thereby impacting the distribution of LNAPL. As a methodological suggestion, future work could incorporate both the real and imaginary parts of permittivity. Using ε′ together with ε″ may offer stronger air–LNAPL contrast.

To mimic a spill scenario LNAPL was infiltrated from the top of the 2D tank, and imbibition and drainage cycles were performed to simulate groundwater table fluctuations. The temperature was raised from 10°C to 20°C after four cycles of drainage and imbibition, and three additional cycles were conducted at 20°C. The key findings are:

- Time domain reflectometries and image analysis showed good agreement in predicting fluid behavior, though image-based saturation values were consistently higher due to the TDR probe’s limited sensitivity to the NAPL phase (2.0 mm vs. 5.0 cm for water). The AI-based Biodock platform effectively detected air bubbles, providing insights into trapped air in the sandwiched and coarse sand zones. Time domain reflectometry probes coupled with image analysis are promising tools for multiphase flow analysis in porous media.

- The main drawback of the TDR probe in such three-phase system is that it cannot accurately differentiate gas from LNAPL solely based on the permittivity. In that regard, image analysis is more reliable, as one can develop a method to detect air bubbles, then discriminate oil from water based on hydrophobic and hydrophilic dyes, and image analysis based on pixel intensity. The main drawback of the image analysis is that the differentiation of the colored phases is based on pixel intensity threshold, which needs some subjectivity in the choice of the threshold value. However, having both TDR and imaging permits dealing with the gas phase and then comparing the outcomes of both TDR and image analysis.
- Porous media heterogeneity (e. g. low-permeable lenses) significantly influenced LNAPL distribution in porous media. LNAPL infiltrated vertically through the low-permeable lens but preferred to flow through the boundaries of permeability transition zones. Lateral movement of LNAPL in coarse sand occurred through interconnected pores, rising in the sandwiched zone, and some LNAPL invaded the saturated zone upon reaching the groundwater table.
- Groundwater table fluctuations affected both vertical and horizontal LNAPL distribution. Imbibition events increased LNAPL entrapment in the capillary fringe, with subsequent imbibition events entrapping more LNAPL. Trapped LNAPL altered the sand grain wettability from water-wet to mixed-oil-wet, as reported in previous studies. After each drainage event, residual LNAPL was observed.
- Temperature changes (from 10°C to 20°C) increased LNAPL mobility by reducing fluid viscosity. While imbibition had no significant effect, drainage after the temperature increase showed less LNAPL in the vadose zone, as LNAPL with

reduced viscosity was more easily mobilized. Image analysis and TDR indicated higher LNAPL saturation after drainage at 20°C compared to 10°C. This highlights the importance of studying the fate and transport of pollutants in the laboratory under temperature conditions relevant to the aquifers.

These findings provide applied guidance for remediation by clarifying how LNAPL migrates and persists in heterogeneous media. Fine-lens heterogeneities act as capillary barriers: during drainage (low water table) LNAPL continuity along the water-table surface increases, improving the potential for hydraulic recovery, whereas during imbibition (high water table), LNAPL partitions into trapped ganglia within the capillary fringe, reducing recoverability. Accordingly, pump-and-treat (or skimming) is likely more efficient when operated at lower water levels or timed to drainage phases, with well-targeted near lens margins. In addition, progressive wettability alteration from water-wet to mixed-wet conditions under prolonged hydrocarbon exposure increases residual saturation and can diminish hydraulic removal efficiency; monitoring and model calibration should explicitly account for this effect.

FIGURES CAPTIONS

Figure 1. Schematical representation of the experimental setup. The numbers indicate the locations of the time domain reflectometry (TDR) probes. The red boxes highlight the areas of interest.

Figure 2. LNAPL infiltration (red color - LNAPL, blue color - water): (A) at the beginning, (B) after 25 minutes, (C) after 95 minutes, (D) 1400 minutes, and (E) permittivity values during LNAPL infiltration.

Figure 3. LNAPL saturation profiles as a function of normalized time (the time in minutes when the image was taken divided by the total number of minutes) at TDR9 zone for 10°C experiments: A) imbibition based on the image, B) imbibition based on TDR, C) drainage based on the image, D) drainage based on TDR.

Figure 4. LNAPL saturation at sandwiched zone for 10°C experiments as a function of normalized time (time in minutes at which image was taken divided to the total time in minutes): A) imbibition based on the image, B) imbibition based on TDR 8, C) drainage based on the image, D) drainage based on TDR 8

Figure 5. 2D tank after temperature changes. Images after A) imbibition 4, B) drainage 4, C) imbibition 5, and D) drainage 5 are displayed with the influence zones of the TDR 8 and 9 in light green rectangles. Temperature increased from 10°C to 20°C after drainage 4.

Figure 6. Saturation profiles for TDR9 zone before (drainage 4) and after (drainage 5) temperature change A) based on permittivity values, B) based on image analysis

REFERENCES

Ajo-Franklin, J. B., Geller, J. T., & Harris, J. M. (2004). The dielectric properties of granular media saturated with DNAPL/water mixtures. *Geophysical Research Letters*, *31*(17), Article 17. https://doi.org/10.1029/2004GL020672

Alamooti, A., Baigadilov, A., Sawadogo, I., Martel, R., Davarzani, D., Ahmadi-Sénichault, A., & Colombano, S. (2025). Mobilization of DNAPL lenses in heterogeneous aquifers using shear-thinning PEO polymers: Experimental and numerical study. *Water Research*, *273*, 122952. https://doi.org/10.1016/j.watres.2024.122952

Alazaiza, M. Y. D., Ramli, M. H., Copty, N. K., Sheng, T. J., & Aburas, M. M. (2020). LNAPL saturation distribution under the influence of water table fluctuations using simplified image analysis method. *Bulletin of Engineering Geology and the Environment*, *79*(3), Article 3. https://doi.org/10.1007/s10064-019-01655-3

Albers, B. (2014). Modeling the hysteretic behavior of the capillary pressure in partially saturated porous media: A review. *Acta Mechanica*, *225*(8), 2163–2189. https://doi.org/10.1007/s00707-014-1122-4

Anderson, W. G. (1986). Wettability Literature Survey- Part 1: Rock/Oil/Brine Interactions and the Effects of Core Handling on Wettability. *Journal of Petroleum Technology*, *38*(10), 1125–1144. https://doi.org/10.2118/13932-pa

Atteia, O., Jousse, F., Cohen, G., & Höhener, P. (2017). Comparison of residual NAPL source removal techniques in 3D metric scale experiments. *Journal of Contaminant Hydrology*, *202*, 23–32. https://doi.org/10.1016/j.jconhyd.2017.04.006

Baigadilov, A., Colombano, S., Omirbekov, S., Cochennec, M., Davarzani, D., Lion, F., Bodiguel, H., & Oxarango, L. (2025). Stability and flow behavior of polymer-enhanced foams for improved in-situ remediation of hydrocarbons: Effect of polymer-surfactant interactions. *Journal of Hazardous Materials*, *486*, 137004. https://doi.org/10.1016/j.jhazmat.2024.137004

Baigadilov, A., Colombano, S., Omirbekov, S., Cochennec, M., Davarzani, D., Lion, F., Oxarango, L., & Bodiguel, H. (2024). Surfactant foam injection for remediation of diesel-contaminated soil: A comprehensive study on the role of co-surfactant in foaming formulation enhancement. *Science of The Total Environment*, *930*, 172631. https://doi.org/10.1016/j.scitotenv.2024.172631

Berry, J. D., Neeson, M. J., Dagastine, R. R., Chan, D. Y. C., & Tabor, R. F. (2015). Measurement of surface and interfacial tension using pendant drop tensiometry. *Journal of Colloid and Interface Science*, *454*, 226–237. https://doi.org/10.1016/j.jcis.2015.05.012

Biodock. (2024). [Computer software]. https://www.biodock.ai/

Blunt, M. J. (2016). *Multiphase Flow in Permeable Media: A Pore-Scale Perspective* (1st ed.). Cambridge University Press. https://doi.org/10.1017/9781316145098

Bradski, G., & Kaehler, A. (2008). *Learning OpenCV: Computer vision with the OpenCV library*. O’Reilly Media, Inc.

Brovelli, A., & Cassiani, G. (2008). Effective permittivity of porous media: A critical analysis of the complex refractive index model. *Geophysical Prospecting*, *56*(5), Article 5. https://doi.org/10.1111/j.1365-2478.2008.00724.x

Cavelan, A., Faure, P., Lorgeoux, C., Colombano, S., Deparis, J., Davarzani, D., Enjelvin, N., Oltean, C., Tinet, A.-J., Domptail, F., & Golfier, F. (2024). An experimental multi-method approach to better characterize the LNAPL fate in soil under fluctuating groundwater levels. *Journal of Contaminant Hydrology*, *262*, 104319. https://doi.org/10.1016/j.jconhyd.2024.104319

Cavelan, A., Golfier, F., Colombano, S., Davarzani, H., Deparis, J., & Faure, P. (2022). A critical review of the influence of groundwater level fluctuations and temperature on LNAPL contaminations in the context of climate change. *Science of The Total Environment*, *806*, 150412. https://doi.org/10.1016/j.scitotenv.2021.150412

Cochennec, M., Davarzani, H., Davit, Y., Colombano, S., Ignatiadis, I., Masselot, G., & Quintard, M. (2022). Impact of gravity and inertia on stable displacements of DNAPL in highly permeable porous media. *Advances in Water Resources*, *162*, 104139. https://doi.org/10.1016/j.advwatres.2022.104139

Colombano, S., Davarzani, H., Van Hullebusch, E. D., Huguenot, D., Guyonnet, D., Deparis, J., & Ignatiadis, I. (2021). Permittivity and electrical resistivity measurements and estimations during the recovery of DNAPL in saturated porous media: 2D tank experiments. *Journal of Applied Geophysics*, *191*, 104359. https://doi.org/10.1016/j.jappgeo.2021.104359

Colombano, S., Davarzani, H., van Hullebusch, E. D., Huguenot, D., Guyonnet, D., Deparis, J., Lion, F., & Ignatiadis, I. (2021a). Comparison of thermal and chemical enhanced recovery of DNAPL in saturated porous media: 2D tank pumping experiments and two-phase flow modelling. *Science of The Total Environment*, *760*, 143958. https://doi.org/10.1016/j.scitotenv.2020.143958

Daučík, P., Višňovský, J., Ambro, J., & Elena, H. (2008). *Temperature Dependence of the Viscosity of Hydrocarbon Fractions*. https://www.researchgate.net/publication/265884437_Temperature_Dependence_of_the_Viscosity_of_Hydrocarbon_Fractions/citations

Dou, Z., Chen, Y., Zhuang, C., Zhou, Z., & Wang, J. (2022). Emergence of non-aqueous phase liquids redistribution driven by freeze-thaw cycles in porous media based on low-field NMR. *Journal of Hydrology*, *612*, 128106. https://doi.org/10.1016/j.jhydrol.2022.128106

Gupta, P. K., Yadav, B., & Yadav, B. K. (2019). Assessment of LNAPL in Subsurface under Fluctuating Groundwater Table Using 2D Sand Tank Experiments. *Journal of Environmental Engineering*, *145*(9), Article 9. https://doi.org/10.1061/(ASCE)EE.1943-7870.0001560

Imhoff, P. T., Frizzell, A., & Miller, C. T. (1997). Evaluation of Thermal Effects on the Dissolution of a Nonaqueous Phase Liquid in Porous Media. *Environmental Science & Technology*, *31*(6), 1615–1622. https://doi.org/10.1021/es960292x

IPCC. (2021). *Climate Change 2021 The Physical Science Basis Summary for Policymakers Working Group I Contribution to the Sixth Assessment Report of the Intergovernmental Panel on Climate Change.* IPCC Geneva.

Iravani, M. A., Davarzani, H., Deparis, J., Colombano, S., Philippe, N., Oniangue, B., Guérin, R., & Maineult, A. (2023). Experimental study of electrical complex resistivity in a 2D multiphase porous medium under non-isothermal conditions: Application to soil remediation monitoring. *Near Surface Geophysics*, *21*(1), 65–81. https://doi.org/10.1002/nsg.12237

Iravani, M. A., Deparis, J., Davarzani, H., Colombano, S., Guérin, R., & Maineult, A. (2020). The influence of temperature on the dielectric permittivity and complex electrical resistivity of porous media saturated with DNAPLs: A laboratory study. *Journal of Applied Geophysics*, *172*, 103921. https://doi.org/10.1016/j.jappgeo.2019.103921

Kechavarzi, C., Soga, K., & Illangasekare, T. H. (2005). Two-dimensional laboratory simulation of LNAPL infiltration and redistribution in the vadose zone. *Journal of Contaminant Hydrology*, *76*(3–4), Article 3–4. https://doi.org/10.1016/j.jconhyd.2004.09.001

Kong, K., & Shao, S. (2023). Effect of wettability on the variation of resistivity characteristics during diesel oil infiltration into the unsaturated zone. *Environmental Earth Sciences*, *82*(23), 552. https://doi.org/10.1007/s12665-023-11254-x

Koohbor, B., Colombano, S., Harrouet, T., Deparis, J., Lion, F., Davarzani, D., & Ataie-Ashtiani, B. (2023). The effects of water table fluctuation on LNAPL deposit in highly permeable porous media: A coupled numerical and experimental study. *Journal of Contaminant Hydrology*, *256*, 104183. https://doi.org/10.1016/j.jconhyd.2023.104183

Kulkarni, P. R., King, D. C., McHugh, T. E., Adamson, D. T., & Newell, C. J. (2017). Impact of Temperature on Groundwater Source Attenuation Rates at Hydrocarbon Sites. *Groundwater Monitoring & Remediation*, *37*(3), 82–93. https://doi.org/10.1111/gwmr.12226

Lenormand, R., Zarcone, C., & Sarr, A. (1983). Mechanisms of the displacement of one fluid by another in a network of capillary ducts. *Journal of Fluid Mechanics*, *135*(1), 337. https://doi.org/10.1017/S0022112083003110

McAlexander, B., & Sihota, N. (2019). Influence of Ambient Temperature, Precipitation, and Groundwater Level on Natural Source Zone Depletion Rates at a Large Semiarid LNAPL Site. *Groundwater Monitoring & Remediation*, *39*(1), 54–65. https://doi.org/10.1111/gwmr.12309

Mehta, D., & Hawley, M. C. (1969). Wall Effect in Packed Columns. *Industrial & Engineering Chemistry Process Design and Development*, *8*(2), 280–282. https://doi.org/10.1021/i260030a021

Newell, C. J. (1995). *Light Non aqueous phase liquids*. https://www.epa.gov/sites/default/files/2015-06/documents/lnapl.pdf

Niţă, I., Osman, S., & Iulian, O. (2021). Dynamic viscosity dependence on temperature for fuels used for diesel engine. *Ovidius University Annals of Chemistry*, *32*(1), 98–103. https://doi.org/10.2478/auoc-2021-0014

Omirbekov, S., Davarzani, H., Colombano, S., & Ahmadi-Senichault, A. (2020). Experimental and numerical upscaling of foam flow in highly permeable porous media. *Advances in Water Resources*, *146*, 103761. https://doi.org/10.1016/j.advwatres.2020.103761

Oostrom, M., Hofstee, C., & Wietsma, T. W. (2006). Behavior of a Viscous LNAPL Under Variable Water Table Conditions. *Soil and Sediment Contamination: An International Journal*, *15*(6), 543–564. https://doi.org/10.1080/15320380600958976

Philippe, N., Davarzani, H., Colombano, S., Dierick, M., Klein, P.-Y., & Marcoux, M. (2020a). Experimental study of the temperature effect on two-phase flow properties in highly permeable porous media: Application to the remediation of dense non-aqueous phase liquids (DNAPLs) in polluted soil. *Advances in Water Resources*, *146*, 103783. https://doi.org/10.1016/j.advwatres.2020.103783

Philippe, N., Davarzani, H., Colombano, S., Dierick, M., Klein, P.-Y., & Marcoux, M. (2020b). Experimental study of the temperature effect on two-phase flow properties in highly permeable porous media: Application to the remediation of dense non-aqueous phase liquids (DNAPLs) in polluted soil. *Advances in Water Resources*, *146*, 103783. https://doi.org/10.1016/j.advwatres.2020.103783

Radke, C. J., Kovscek, A. R., & Wong, H. (1992). A Pore-Level Scenario for the Development of Mixed Wettability in Oil Reservoirs. *SPE Annual Technical Conference and Exhibition,* SPE-24880-MS. https://doi.org/10.2118/24880-MS

Riley, F. (2013). *The electronics assembly handbook.* Springer Science & Business Media.

Rivett, M. O., Tomlinson, D. W., Thornton, S. F., Thomas, A. O., Leharne,., S. A., & Wealthall, G. P. (2014). *An Illustrated Handbook of LNAPL Transport and Fate in the Subsurface*.

Rosenbaum, U., Huisman, J. A., Vrba, J., Vereecken, H., & Bogena, H. R. (2011). Correction of Temperature and Electrical Conductivity Effects on Dielectric Permittivity Measurements with ECH$_2$ O Sensors. *Vadose Zone Journal*, *10*(2), 582–593. https://doi.org/10.2136/vzj2010.0083

Sabyrbay, B., Davarzani, D., Colombano, S., Omirbekov, S., Kodebay, I., Lorthioy, M., Krimissa, M., & Dicharry, C. (2025). Enhanced remediation of diesel-contaminated soils using a novel biopolymer-based emulsion. *Journal of Hazardous Materials*, *492*, 138183. https://doi.org/10.1016/j.jhazmat.2025.138183

Sabyrbay, B., Davarzani, D., Dicharry, C., Omirbekov, S., Lion, F., Alamooti, A., Lorthioy, M., Krimissa, M., & Colombano, S. (2025). Assessment of a novel alcohol-in-biopolymer emulsion for enhanced remediation of diesel-contaminated soils. *Journal of Hazardous Materials Advances*, *18*, 100616. https://doi.org/10.1016/j.hazadv.2025.100616

Sleep, B. E., & Ma, Y. (1997). Thermal variation of organic fluid properties and impact on thermal remediation feasibility. *Journal of Soil Contamination*, *6*(3), 281–306. https://doi.org/10.1080/15320389709383566

Tomlinson, D. W., Rivett, M. O., Wealthall, G. P., & Sweeney, R. E. H. (2017). Understanding complex LNAPL sites: Illustrated handbook of LNAPL transport and fate in the subsurface. *Journal of Environmental Management*, *204*, 748–756. https://doi.org/10.1016/j.jenvman.2017.08.015

Whitaker, S. (1986). Flow in porous media II: The governing equations for immiscible, two-phase flow. *Transport in Porous Media*, *1*(2), 105–125. https://doi.org/10.1007/BF00714688

Williams, M. G., Faber, Z. J., & Kelley, T. J. (2025). Comparison of artificial intelligence image processing with manual leucocyte differential to score immune cell infiltration in a mouse infection model of cystic fibrosis. *Journal of Pathology Informatics*, *17*, 100438. https://doi.org/10.1016/j.jpi.2025.100438

Wipfler, E. L., Ness, M., Breedveld, G. D., Marsman, A., & Van Der Zee, S. E. A. T. M. (2004). Infiltration and redistribution of LNAPL into unsaturated layered porous media. *Journal of Contaminant Hydrology*, *71*(1–4), 47–66. https://doi.org/10.1016/j.jconhyd.2003.09.004

Yimsiri, S., Euaapiwatch, S., Flores, G., Katsumi, T., & Likitlersuang, S. (2018). Effects of water table fluctuation on diesel fuel migration in one-dimensional laboratory study. *European Journal of Environmental and Civil Engineering*, *22*(3), 359–385. https://doi.org/10.1080/19648189.2016.1197158

Zhao, G., Cheng, J., Jia, M., Zhang, H., Li, H., & Zhang, H. (2024). The Effect Characterization of Lens on LNAPL Migration Based on High-Density Resistivity Imaging Technique. *Applied Sciences*, *14*(22), 10389. https://doi.org/10.3390/app142210389

Zuo, R., Zhao, X., Yang, J., Pan, M., Xue, Z., Gao, X., Wang, J., & Teng, Y. (2021). Analysis of the LNAPL Migration Process in the Vadose Zone under Two Different Media Conditions. *International Journal of Environmental Research and Public Health*, *18*(21), 11073. https://doi.org/10.3390/ijerph182111073

TABLES

Table 1. Measured porous media properties for the fine and coarse sands.

Sand type	**Grain size range, mm**	**Porosity**	**Permeability, 10^{-12} m^2**
Coarse sand	1-1.25	0.37-0.40	562 ± 22
Fine sand	0.1-0.35		26 ± 2

Table 2. Relative permittivity ε of air, LNAPL, and water at different temperatures

Temperature, °C	ε_{air}	ε_{diesel}	ε_{water}
10	1.3	2.7	37.7
15	1.4	2.8	36.0
21	1.4	2.9	35.6
25	1.4	3.0	34.2
30	1.5	3.0	32.8

Table 3. Viscosity and interfacial tension of LNAPL and LNAPL-water at studied temperatures

Temperature, °C	**Viscosity, mPa·s**	**Interfacial tension, mN m^{-1}**

10	4.03 ± 0.02	15.8 ± 1.1
20	3.39 ± 0.03	15.4 ± 1.4

Table 2. Capillary number and viscosity ratio for the LNAPL-water pair for drainage and imbibition at 10 and 20°C

Temperature, °C	**Process**	**Capillary number**	**Viscosity ratio**
10	imbibition	1.2E-7	0.3
	drainage	3.6E-7	3.1
20	imbibition	9.2E-8	0.3
	drainage	3.1E-7	3.4